

---

# First-Passage Time Statistics on Surfaces of General Shape: Surface PDE Solvers using Generalized Moving Least Squares (GMLS)

B. J. Gross<sup>1,2</sup>, P. Kuberry<sup>3</sup>, P. J. Atzberger<sup>1,2</sup>

[1] Department of Mathematics, University of California Santa Barbara (UCSB);

[2] Department of Mechanical Engineering, University of California Santa Barbara (UCSB);

[3] Sandia National Laboratories, Albuquerque, NM \*\*

atzberg@gmail.com; <http://atzberger.org/>

---

**W**e develop numerical methods for computing statistics of stochastic processes on surfaces of general shape with drift-diffusion dynamics  $d\mathbf{X}_t = a(\mathbf{X}_t)dt + \mathbf{b}(\mathbf{X}_t)d\mathbf{W}_t$ . We consider on a surface domain  $\Omega$  the statistics  $u(\mathbf{x}) = \mathbb{E}^{\mathbf{x}} [\int_0^\tau g(X_t)dt] + \mathbb{E}^{\mathbf{x}} [f(X_\tau)]$  with the exit stopping time  $\tau = \inf_t \{t > 0 \mid X_t \notin \Omega\}$ . Using Dynkin's formula, we compute statistics by developing high-order Generalized Moving Least Squares (GMLS) solvers for the associated surface PDE boundary-value problems. We focus particularly on the mean First Passage Times (FPTs) given by the special case  $f = 0, g = 1$  with  $u(\mathbf{x}) = \mathbb{E}^{\mathbf{x}} [\tau]$ . We perform studies for a variety of shapes showing our methods converge with high-order accuracy both in capturing the geometry and the surface PDE solutions. We then perform studies showing how FPTs are influenced by the surface geometry, drift dynamics, and spatially dependent diffusivities.

## Introduction

First Passage Times (FPTs) [3, 12, 15] are of interest in many problems arising in fields including biology [28, 31, 34, 38, 40], physics [6, 8, 33, 42, 43, 49], engineering [20, 36, 46], finance [1, 22, 26, 30], and machine learning [21, 51]. We consider here FPTs in the case of Ito stochastic processes  $\mathbf{X}_t$  with dynamics  $d\mathbf{X}_t = a(\mathbf{X}_t)dt + \mathbf{b}(\mathbf{X}_t)d\mathbf{W}_t$ , [4, 12]. While stochastic numerical methods are available for approximating and sampling trajectories  $\{X_t\}_{0 \leq t \leq T}$ , [7], this can be computationally expensive given disparate dynamical time-scales and statistical sampling errors [4, 8, 34]. In practice, often of primary interest are a subset of statistics for characterizing underlying behaviors or for making predictions of observations or measurements. We consider here the class of statistics for  $\mathbf{X}_t$  on an open domain  $\Omega$  of the form  $u(\mathbf{x}) = \mathbb{E}^{\mathbf{x}} [\int_0^\tau g(X_t)dt] + \mathbb{E}^{\mathbf{x}} [f(X_\tau)]$  with the exit stopping time  $\tau = \inf_t \{t > 0 \mid X_t \notin \Omega\}$ . Through the choice of  $g$ , this provides information about the states  $x \in \Omega$  realized by the stochastic trajectories. Through the choice of  $f$ , information is obtained about where stochastic trajectories encounter the boundary  $\partial\Omega$ . The Dynkin formula provides a connection between these statistics and a collection of elliptic Partial Differential Equations (PDEs) with boundary-value problems of the form  $\mathcal{L}u = -g, \mathbf{x} \in \Omega, u = f, \mathbf{x} \in \partial\Omega$ , [12].

For many problems, it is useful to consider stochastic processes  $\mathbf{X}_t$  in the manifold setting allowing for non-trivial topology or geometry [29, 33, 37, 43, 47]. We consider the case of stochastic processes  $\mathbf{X}_t$  within general surfaces, having potentially complicated shapes. We develop high-order methods for numerically computing statistics from the PDE boundary-value problems using Generalized Moving Least Squares (GMLS) approximations [17, 25]. Our approach provides meshless

---

\* Work supported by DOE Grant ASCR PhILMS DE-SC0019246 and NSF Grant DMS-1616353. Page 1 of 24

\*\*Sandia National Laboratories is a multi-mission laboratory managed and operated by National Technology and Engineering Solutions of Sandia, LLC., a wholly owned subsidiary of Honeywell International, Inc., for the U.S. Department of Energy's National Nuclear Security Administration under contract DE-NA0003525. This paper describes objective technical results and analysis. Any subjective views or opinions that might be expressed in the paper do not necessarily represent the views of the U.S. Department of Energy or the United States Government. SAND2021-XXXX J

methods for solving PDEs on surfaces related to [19, 27, 45, 52, 53]. We focus particularly on the mean first passage times given by the special case  $f = 0$ ,  $g = 1$  with  $u(\mathbf{x}) = \mathbb{E}^{\mathbf{x}}[\tau]$ . We perform studies for a variety of shapes to investigate how our methods converge. We show our methods can achieve high-order accuracy both in capturing the geometry and the solutions of the surface PDEs. We show how our methods can be utilized to investigate the behaviors of stochastic processes having drift-diffusion dynamics confined to surfaces. We perform studies for how FPTs are affected by surface geometry, drift dynamics, and spatially dependent diffusivities. Our methods can also be used for computing other path-dependent statistics of stochastic processes confined to surfaces of general shape.

## 1. First-Passage Times and Path-Dependent Statistics on Surfaces

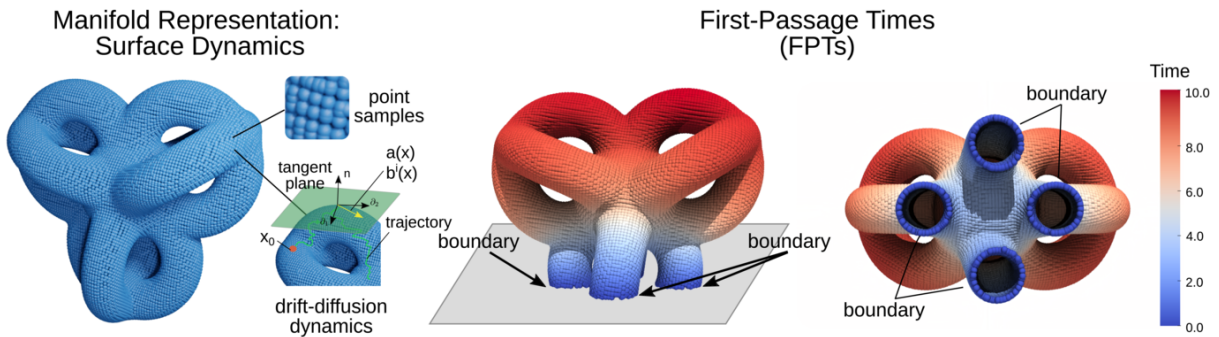


**Figure 1.:** (left) The mean First-Passage-Times (FPT) can be computed using our methods for manifold surfaces having a general shape with potentially complicated geometry or topology. Starting  $\mathbf{X}_t$  at any location  $\mathbf{X}(0) = \mathbf{x}_0$  on the surface, the FPT is obtained by computing the average arrival time at the boundary created by slicing the surface at  $z = 0$ . The manifold surface is represented by a collection of point samples. (right) The FPT is indicated by the color at location  $\mathbf{x}_0$  on the surface. Our methods allow for computing FPTs for stochastic processes with general drift-diffusion dynamics  $d\mathbf{X}_t = \mathbf{a}(\mathbf{X}_t)dt + \mathbf{b}(\mathbf{X}_t)d\mathbf{W}_t$ . We show here results in the diffusive case with  $\mathbf{a}(x) = 0$  and  $\mathbf{b}(x) = I$ .

The mean First-Passage Time (FPT) is defined as

$$u(\mathbf{x}_0) = \mathbb{E}^{X(0)=\mathbf{x}_0}[\tau], \quad \text{where } \tau = \inf\{t > 0 \mid X_t \notin \Omega\}. \quad (1)$$

This gives the time  $\tau$  for a particle starting at location  $X(0) = \mathbf{x}_0 \in \Omega$  to reach the boundary of the domain  $\partial\Omega$ . We denote by  $u(\mathbf{x}_0)$  the average value of this passage time. In Figure 1, we show the case of a manifold surface with boundary defined by a cut-plane at  $z = 0$ . The color at  $\mathbf{x}$  indicates  $u(\mathbf{x})$  for the mean first passage time for a diffusion on the surface starting at  $\mathbf{x}$  to reach the boundary at  $z = 0$ , see Figure 1.

We consider general drift-diffusion dynamics constrained to a surface  $\mathcal{M}$  governed by the Stochastic Differential Equations (SDEs), [12]

$$d\mathbf{X}_t = \mathbf{a}(\mathbf{X}_t)dt + \mathbf{b}(\mathbf{X}_t)d\mathbf{W}_t, \quad (2)$$

subject to  $\mathbf{X}_t \in \mathcal{M}$ .

The  $\mathbf{a}$  term models drift in the dynamics and  $\mathbf{b}$  the diffusive contributions. Throughout, we interpret our SDEs in terms of Ito stochastic processes [12].

While in principle stochastic simulations can be performed to compute sample trajectories for Monte-Carlo estimates of statistics, in practice this can be expensive given disparate time-scales in the dynamics and the slow decay of statistical errors [10, 34]. We develop alternative approaches using Dynkin's formula [12] which relates FPTs and other path-dependent statistics to Partial Differential Equations (PDEs). We develop solvers for these associated boundary-value problems.

For the stochastic process  $\mathbf{X}_t$ , we consider path-dependent statistics  $u$  of the form

$$u(\mathbf{x}) = \mathbb{E}^{\mathbf{x}} \left[ \int_0^\tau g(\mathbf{X}_t) dt \right] + \mathbb{E}^{\mathbf{x}} [f(\mathbf{X}_\tau)]. \quad (3)$$

The  $g(x)$  allows us to assign a value to individual trajectories based on the locations they traverse inside the domain  $x \in \Omega$  and  $f(x)$  to assign a cost for the location where the process hits the boundary  $x \in \partial\Omega$ . The Dynkin formula for  $q(x)$  is given by [12]

$$\mathbb{E}^{\mathbf{x}} [q(X_\tau)] = q(x) + \mathbb{E}^{\mathbf{x}} \left[ \int_0^\tau \mathcal{L}q(X_s) ds \right]. \quad (4)$$

The  $\mathcal{L}$  is the Infinitesimal Generator associated with the SDE in equation 2 which can be expressed as the differential operator

$$\mathcal{L} = \mathbf{a} \cdot \frac{\partial}{\partial \mathbf{x}} + \frac{1}{2} \mathbf{b} \mathbf{b}^T : \frac{\partial^2}{\partial \mathbf{x}^2}. \quad (5)$$

Here, the  $\cdot$  denotes the usual dot product with a gradient, and the  $:$  denotes the Hadamard element-wise dot product (tensor contraction over indices). We take  $q(x) = f(x)$ ,  $x \in \partial\Omega$  and  $\mathcal{L}q(x) = -g(x)$ ,  $x \in \Omega$ . After rearranging terms, we have formally  $u(x) = q(x)$ ,  $x \in \bar{\Omega}$ . Using this and equation 5, we can express the statistic  $u$  as the solution of a surface elliptic PDE of the form

$$\mathcal{L}u = -g, \quad \mathbf{x} \in \Omega \quad u = f, \quad \mathbf{x} \in \partial\Omega, \quad (6)$$

where  $\mathcal{L}$  is given in equation 5. We require throughout  $f \in C_0^2(\partial\Omega)$  and  $g \in C_0^2(\Omega)$ .

In the special case with  $f = 0$  and  $g = -1$ , we obtain the mean first-passage time

$$u(\mathbf{x}) = \mathbb{E}^{\mathbf{x}} [\tau], \quad \tau = \inf\{t | X_t \neq \Omega\}. \quad (7)$$

This is the amount of time on average it takes for the drift-diffusion process starting at location  $\mathbf{x}$  to hit the boundary of the domain  $\partial\Omega$ .

To compute these and other path-dependent statistics for stochastic processes constrained to surfaces, we develop solvers for the surface PDEs of equation 6. We show how these methods can be used to investigate the roles played by geometry and the drift-diffusion dynamics modeled by  $\mathbf{a}$  and  $\mathbf{b}$  in first-passage times and the path-dependent statistics of equation 3.

## 1.1. Stochastic Processes and Drift-Diffusion Dynamics on Surfaces

We consider general surface drift-diffusion dynamics associated with Ito stochastic processes of the form

$$d\mathbf{X}_t = \mathbf{a} dt + \mathbf{b} d\mathbf{W}_t. \quad (8)$$

The  $\mathbf{X}_t \in \mathbb{R}^n$  defines the location in terms of the ambient space. The  $\mathbf{a}(\mathbf{x}) \in \mathbb{R}^n$  and  $\mathbf{b}(\mathbf{x}) \in \mathbb{R}^{n \times m}$ . In the embedding space we assume the drift  $\mathbf{a}$  is in the tangent plane at each point  $\mathbf{a}(\mathbf{x}) \in T\mathcal{M}_{\mathbf{x}}$  and that the range of the diffusion tensor  $\mathbf{b}$  is in the tangent space  $\text{range}(\mathbf{b}) \subset T\mathcal{M}_{\mathbf{x}}$ . As a result, the null-space of  $\mathbf{b}^T$  is the space of vectors orthogonal to the tangent space  $T\mathcal{M}_{\mathbf{x}}$ . This has the consequence that  $\mathbf{b}\mathbf{b}^T$  has a null-space of vectors orthogonal to the tangent space and the range of vectors spanned by  $\mathbf{b}$  in the tangent space.

In modeling systems, it is often convenient to specify the drift and diffusion using the embedding space representations of  $\mathbf{a}$  and  $\mathbf{b}$ . In numerical methods and when performing other practical calculations, it is often convenient to express the dynamics using local coordinate charts  $\mathbf{q} = (q_1, q_2)$  with embedding map  $\mathbf{x} = \boldsymbol{\sigma}(q_1, q_2)$ . It will be convenient to have ways to convert between these types of descriptions. The drift-diffusion dynamics in a local coordinate chart can be expressed as the Ito stochastic process

$$d\mathbf{q}_t = \boldsymbol{\alpha}dt + \boldsymbol{\beta}d\tilde{\mathbf{W}}_t, \quad (9)$$

where  $\boldsymbol{\alpha}(\mathbf{q}) \in \mathbb{R}^2$  and  $\boldsymbol{\beta}(\mathbf{q}) \in \mathbb{R}^{2 \times \tilde{m}}$  with  $\tilde{m}$  the number of noise sources.

These descriptions are connected through the embedding map  $\boldsymbol{\sigma}$  given by  $\mathbf{X} = \boldsymbol{\sigma}(\mathbf{q})$ . Using the Ito Lemma [12], we can connect the dynamics in the embedding space with those in the coordinate chart by

$$d\mathbf{X}_t = \left[ \alpha^a + \frac{1}{2} \Gamma_{ij}^a \beta^i \beta^{j,T} \right] \boldsymbol{\sigma}_{q^a} dt + \boldsymbol{\sigma}_{q^a} \beta^a d\tilde{\mathbf{W}}_t. \quad (10)$$

The  $\Gamma_{ij}^a$  are the Christoffel symbols of the surface. Note that  $\beta^a \in \mathbb{R}^2$  is a row vector and  $d\tilde{\mathbf{W}}_t \in \mathbb{R}^2$ , so combining give a scalar for the coordinate component. In this notation we use the convention that  $\partial_{q^a} = \partial\boldsymbol{\sigma}/\partial q^a = \boldsymbol{\sigma}_{q^a}$ . We also use here the repeated index summation convention. This provides a way to build up in terms of the components of the basis  $\{\partial_{q^a}\}_a$  the dynamics of  $\mathbf{X}_t$  in the embedding space.

We obtain relations between descriptions using the expressions for the dynamics in the embedding space  $\mathbb{R}^3$  and the dynamics expressed in the coordinates  $\mathbf{q}$ . These can be summarized as follows

$$\mathbf{b}\mathbf{b}^T = \beta^a \beta^{b,T} \partial_{q^a} \partial_{q^b}^T = \beta^a \beta^{b,T} \boldsymbol{\sigma}_{q^a} \boldsymbol{\sigma}_{q^b}^T, \quad a^c = g^{cb} \langle \mathbf{a}, \boldsymbol{\sigma}_{q^b} \rangle_g, \quad \alpha^c = a^c - \frac{1}{2} \Gamma_{ab}^c \beta^a \beta^{b,T}. \quad (11)$$

The  $\beta^a \beta^{b,T}$  is a scalar, since  $\beta^c$  is a row vector. The  $\langle \cdot, \cdot \rangle_g$  denotes the inner-product in the embedding space. The  $a^c$  is useful so that we can represent the vector as  $\mathbf{a} = a^c \boldsymbol{\sigma}_{q^c}$ . We still subscript with  $g$  even in the embedding space to highlight that this corresponds to the metric inner-product when using a coordinate chart. In practice, this is computed readily if we represent the vectors in the ambient space as the usual Euclidean inner-product between vectors. While there are many possible choices of the noise terms  $\boldsymbol{\beta}$  and  $\mathbf{b}$  consistent with these equations, each are weakly equivalent since they have the same marginal probability densities. For convenience, we make the specific choice

$$\mathbf{b} = \boldsymbol{\sigma}_{q^a} \beta^a. \quad (12)$$

This can be verified to satisfy the relations above.

The  $\sigma_{q^a}$  is a column vector and  $\beta^a$  is a row vector so that  $\mathbf{b}$  is a  $2 \times 2$  matrix. We choose also for our driving Brownian motion here  $W_t = \tilde{W}_t$  with  $m = \tilde{m} = 2$ . With this correspondence, we also can express  $\beta^a$  in terms of  $\mathbf{b}$  as

$$\sigma_{q^b}^T \mathbf{b} = \sigma_{q^b}^T \sigma_{q^a} \beta^a = g_{ab} \beta^a. \quad (13)$$

This can be solved using the inverse metric tensor as

$$\beta^c = g^{cb} \sigma_{q^b}^T \mathbf{b}. \quad (14)$$

The  $\sigma_{q^b}^T$  is a row vector,  $\mathbf{b}$  is a matrix, and this yields the row vector  $\beta^c$ .

We can substitute this in equation 11 to relate the coordinate chart drift and diffusion terms to the embedding space quantities as

$$\beta^c = g^{cb} \sigma_{q^b}^T \mathbf{b}, \quad a^c = g^{cb} \langle \mathbf{a}, \partial_{q^b} \rangle_g, \quad \alpha^c = a^c - \frac{1}{2} \Gamma_{ab}^c \beta^a \beta^{b,T}. \quad (15)$$

The Infinitesimal Generator  $\mathcal{L}$  for the surface drift-diffusion process in equation 5 can be expressed in the local coordinate chart as

$$\mathcal{L}u = \alpha^c \frac{\partial u}{\partial q^c} + \frac{1}{2} \beta^c \beta^{d,T} \frac{\partial^2 u}{\partial q^c \partial q^d}. \quad (16)$$

In practice, this is used to compute the action of  $\mathcal{L}$  on  $u$  when evaluating terms in the surface PDEs in equation 6.

We remark that a convenient feature of these calculations is that in the final expressions no derivatives of the drift and diffusion coefficients were needed. This is particularly helpful on complicated surfaces for practical calculations. For modeling and simulation in practice, we use the convention for the data structures that  $\mathbf{a}$  is given as a vector field on the point cloud. We also specify that  $\mathbf{b}$  is given in terms of components  $\mathbf{b}[1], \mathbf{b}[2], \mathbf{b}[3]$ , where  $\mathbf{b}[i]$  is the  $i^{th}$  column of the matrix. In this way, we can represent readily the tensors  $\mathbf{a}, \mathbf{b}$  and terms needed in the calculations of  $\mathcal{L}$  using equations 15 and 16 when solving equation 6.

## 2. GMLS Solvers for Surface Partial Differential Equations (PDEs)

To obtain first passage times and other path-dependent statistics, we need numerical methods for solving the elliptic surface PDEs in equation 6. This requires approximation of the surface geometry and associated differential operators arising in equations 6, 15, and 16. This poses challenges given the high-order derivatives required of geometric quantities such as the local surface curvature and metric tensor. We address this by developing meshless approaches based on Generalized Moving Least Squares (GMLS) [17, 25]. We use this to obtain high-order approximations for geometric quantities associated with the local surface geometry facilitating the calculation of the needed derivatives. In meshless methods a collection of point samples is used to represent the manifold geometry and location of approximated surface field values, see Figure 2. We develop GMLS approaches for estimating both local geometric quantities and differential operators to approximate the action of the surface operators and to build collocation methods for the PDEs.

## 2.1. Generalized Moving Least Squares (GMLS) Approximation

The manifold is represented as a point cloud  $\{x_i\}_{i=1}^N$  from which we need to approximate associated differential operators and geometric quantities. Generalized Moving Least Squares (GMLS) approximates operators of the underlying surface fields by solving a collection of local least-squares problems [17, 25]. For a Banach space  $\mathbb{V}$  with dual space  $\mathbb{V}^*$  defined at each  $x_i$ , an approximation is sought for a target operator  $\tau_{x_i}[u]$ , where  $\tau_{x_i} \in \mathbb{V}^*$  and  $u(x) \in \mathbb{V}$  for  $x \in \Omega \subset \mathbb{R}^d$  where  $\Omega$  is a compact domain. In practice, we take  $\mathbb{V} = \mathbb{V}_n$  to be a collection of polynomials up to degree  $n$ . We relate  $u \in \mathbb{V}$  to a representative  $p^* \in \mathbb{V}_n$ , by considering a collection of linear functionals  $\Lambda = \{\lambda_j\}_{j=1}^N$  that serve to characterize  $u$  by  $\Lambda[u] = (\lambda_1[u], \lambda_2[u], \dots, \lambda_N[u])$ . We construct the approximation  $p^*$  by solving the  $\ell^2$ -optimization problem

$$p^* = \arg \min_{p \in \mathbb{V}_n} \sum_{j=1}^N (\lambda_j[u] - \lambda_j[p])^2 \omega(\lambda_j, \tau_{x_i}). \quad (17)$$

The  $\omega(\lambda_j, \tau_{x_i})$  provides weights characterizing the importance of the particular sampling function  $\lambda_j$  in estimating  $\tau_{x_j}$ . For example, we can take  $\lambda_j = \delta(x - x_j)$  with  $\lambda_j[u] = u(x_j)$  and we can take  $\omega(\lambda_j, \tau_{x_i}) = \omega(x_j - x_i)$  to be a function that decays as the distance increases between  $x_j$  and  $x_i$ . We can further take  $\omega = \omega(\|x_j - x_i\|)$  to be a radial function that decays to zero when  $r > \epsilon$ . In practice, we use  $\omega(\|x_j - x_i\|) = (1 - \|x_j - x_i\|/\epsilon)_+^p$  where  $(\cdot)_+ = \max(\cdot, 0)$ .

Consider a basis of functions  $\Phi = \{\phi_i\}_{i=1}^{d_n}$  for  $\mathbb{V}_n$  so that  $\mathbb{V}_n = \text{span}\{\phi_1, \phi_2, \dots, \phi_{d_n}\}$  with  $d_n = \dim \mathbb{V}_n$ . Any function  $p \in \mathbb{V}_n$  now can be expressed as

$$p(x) = \Phi^T \mathbf{a} = \sum_{i=1}^{d_n} a_i \phi_i(x). \quad (18)$$

Let  $\tau[\Phi]$  denote a vector where the components are the target operator acting on each of the basis elements. For the the target operator  $\tau$ , we obtain the GMLS approximation  $\tilde{\tau}$  by considering how  $\tau$  acts on the optimal reconstruction  $p^* = \Phi^T \mathbf{a}^*$  of  $u$ ,

$$\tilde{\tau}[u] := \tau[p^*] = \tau[\Phi]^T \mathbf{a}^*. \quad (19)$$

Conditions ensuring the existence of solutions to equation 17 depend primarily on the unisolvency of  $\Lambda$  over  $\mathbb{V}$  and distribution of the point samples  $\{x_i\}$ . For theoretical results related to GMLS see [17, 25]. GMLS has been primarily used to obtain approximations of constant coefficient linear differential operators [17].

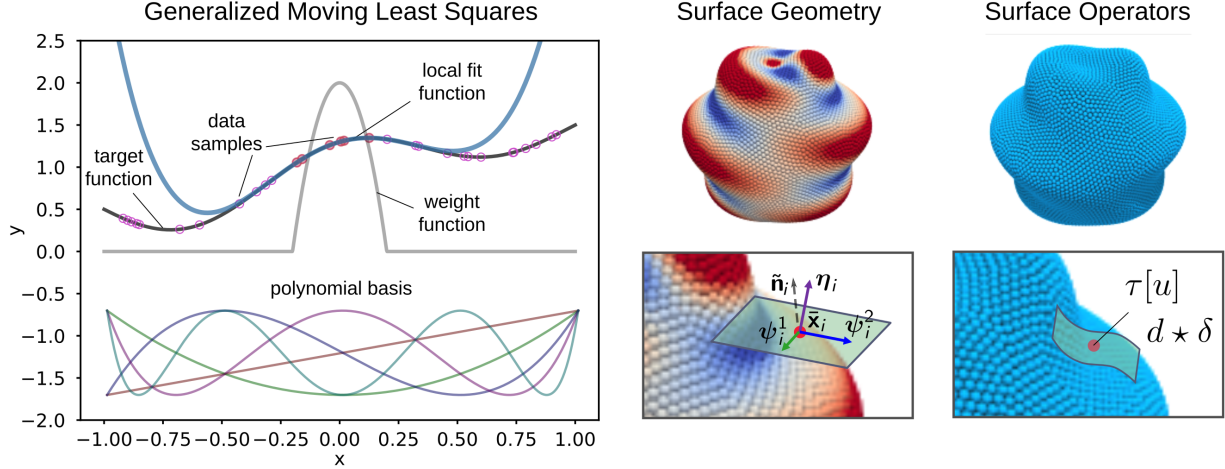


**Figure 2.: Generalized Moving Least Squares (GMLS) on Surfaces.** (left) For general surfaces, we approximate the geometry and the action of operators  $\tau[u]$  using variants of Moving Least Squares (MLS). To approximate a target function  $u(x)$  in the neighborhood of a given point  $x^*$ , Generalized Moving Least Squares (GMLS) uses data samples  $\{(x_j, u(x_j))\}_{j=1}^m$  and probing functionals  $\{\lambda_k[u]\}$  to select a local fit  $p^* = p^*(x; x^*) \in \mathbb{V}$ . For the function space  $\mathbb{V}$ , we use throughout multivariate polynomials. (middle) A local approximation to operators is obtained by solving a local least-squares problem with data weighted by the function  $w(x^*, x_j)$  using equations 17 and 19. By using Principle Component Analysis (PCA) to find at  $x^*$  an approximate local tangent plane and using MLS in the Monge-Gauge, we can estimate surface geometric quantities such as the Gaussian curvature. (right) This approach is generalized further to estimate the action of surface operators  $\tau[u]$ , including the exterior derivative  $d$ , co-differential  $\delta$ , Hodge star  $\star$ , and other surface operators, see Appendix A.

For our first-passage time problems, the target operators are technically non-linear given their dependence on the geometry of the underlying manifold which also must be estimated from the point cloud. We handle this using a two stage approximation approach. In this first stage, we use the point cloud to estimate two basis vectors  $\psi_1$  and  $\psi_2$  for the local tangent plane using Principle Component Analysis (PCA) [2, 13]. We use these basis vectors to construct a local coordinate chart  $(q_1, q_2)$ . In this chart, we fit a function  $p^* \in \mathbb{V}$  to the local point cloud to obtain a Monge-Gauge [14] representation of the surface  $(q_1, q_2, p^*(q_1, q_2))$ . We use GMLS to estimate target geometric quantities of interest, such as the local Gaussian curvature or high-order derivatives. In the second stage, we use the estimated geometric quantities to specify the target operators  $\tau[u]$  for the fields  $u$ . We then use again GMLS to obtain an approximation of  $\tilde{\tau}$  and to compute numerically the target operator values at  $\mathbf{x}_i$ . We have used related procedures for solving hydrodynamic equations on manifolds in [52]. We illustrate the approximation approach in Figure 2.

## 2.2. Numerical Methods for Solving the Surface PDEs

To compute numerically the first passage times, we develop solvers for the elliptic PDE boundary value problems given in equation 6. This is organized by representing the  $f$  and  $g$  function inputs and the  $\mathbf{a}$  and  $\mathbf{b}$  fields specifying the drift-diffusion dynamics. To avoid complications with local coordinate charts, we numerically represent all input data globally using the ambient embedding

space coordinates  $\mathbf{x} \in \mathbb{R}^3$ . The  $\mathbf{a} \in \mathbb{R}^3$  with only the tangential components playing a role in practice. Similarly, the  $\mathbf{b}$  tensor is represented by three vector fields  $\mathbf{b}_1$ ,  $\mathbf{b}_2$ , and  $\mathbf{b}_3$ . We use labels on the point cloud to determine which regions are to be considered interior to  $\Omega$  and which are part of the boundary of  $\partial\Omega$ . We only require  $f$  to be evaluated on  $\partial\Omega$ , while  $g$  must return reliable values for all  $\mathbf{x} \in \Omega$ .

We use our GMLS methods in section 2.1 to estimate the surface geometric quantities and the action of the operator in equation 6. This allows us to construct at each  $\mathbf{x}_i$  an equation for relating  $\mathcal{L}u(\mathbf{x}_i) = -g(\mathbf{x}_i)$ . This provides our collocation method for determining  $u(\mathbf{x}_i)$ . Let  $[\tilde{u}]_i = u(\mathbf{x}_i)$  and  $[\tilde{g}]_i = g(\mathbf{x}_i)$ . Collecting these equations together gives a sparse linear system  $A\tilde{\mathbf{u}} = \tilde{\mathbf{g}}$ . We solve this large sparse linear system using GMRES with algebraic multigrid (AMG) preconditioning using Trilinos [18]. Our solvers have been implemented within a framework for GMLS problems using the Compadre library and PyCompadre [50]. The toolkit provides domain decomposed distributed vector representation of fields as well as global matrix assembly. The capability of the library were also extended for our surface geometry calculations by implementing symbolically generated target operators. Our methods also made use of the iterative block solvers of (Belos [24]), block preconditioners of (Teko) and the AMG preconditioners of (MueLu [32, 35]) within the Trilinos software framework [18]. The framework facilitates developing a scalable implementation of our methods providing ways to use sparse data structures, parallelization, and hardware accelerations.

### 3. Convergence Results

We investigate the convergence of our GMLS solvers developed in section 2. The target operators that arise in the surface PDE boundary-value problems involve a non-linear approximation. This arises from the coupling between the contributions to the error from the differential terms of the surface operators and the GMLS estimations used for the surface geometry.

#### 3.1. Surface Geometries for Validation Studies

We perform studies using four different surface geometries: (i) ellipsoid, (ii) radial manifold I, (iii) radial manifold II, and (iv) torus. We label these as Manifold A–D, see Figure 3. We study convergence as the surface point sampling is refined. We take each refinement to have approximately four times the number of points as the previous level. This aims to have the fill distance  $h$  halve under each refinement.

The manifolds can be described by the following implicit equations. Manifold A is an ellipsoid defined by the equation  $x^2/a^2 + y^2/b^2 + z^2 = s_0^2$  with  $a = 1.2, b = 1.2, s_0^2 = 1$ . Manifold B is a radial manifold defined in spherical coordinates by  $(\theta, \phi, r(\theta, \phi))$  where  $r(\theta, \phi) = 1 + r_0 \sin(3\phi) \cos(\theta)$  with  $r_0 = 0.1$ . Manifold C is a radial manifold defined in spherical coordinates by  $(\theta, \phi, r(\theta, \phi))$  where  $r(\theta, \phi) = 1 + r_0 \sin(7\phi) \cos(\theta)$  with  $r_0 = 0.1$ . Manifold D is a torus defined by the equation  $(s_1^2 - \sqrt{x^2 + y^2})^2 + z^2 = s_2^2$  with  $s_1^2 = 0.7, s_2^2 = 0.3$ . Each of the manifolds shown are represented by quasi-uniform point sets with approximately  $n = 10^4$  samples. For quasi-uniform sampling we expect the fill-distance  $h$  to scale as  $h \sim 1/\sqrt{n}$ . We report our results throughout using the notation  $\bar{h}^{-1} = \sqrt{n}$ . Additional information on the number  $n$  used in samplings can be found in Appendix D.

In our first passage time calculations, unless indicated otherwise, we generate the boundary  $\partial\Omega$  as the points at  $z = 0$ . In practice, we treat any points with  $|z| < 4 \times 10^{-2}$  as boundary points.



This serves to thicken the boundary region and at points  $\mathbf{x}_i$  near the boundary  $\partial\Omega$  helps achieve unisolvency in the local least-squares problems.

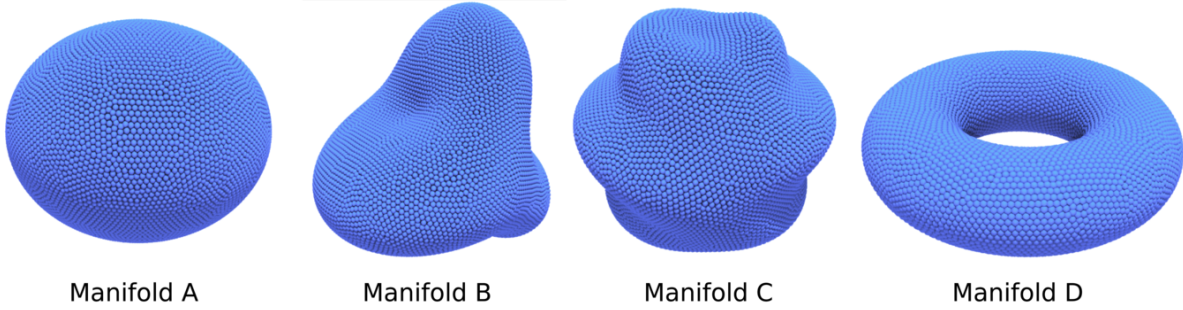


**Figure 3.:** *Point Sample Representations of the Surface Manifolds.*

### 3.2. Test Fields and Manufactured Solutions

We study the accuracy of our GMLS approximations of the surface operators by investigating their action on test fields  $\hat{\mathbf{u}}(\mathbf{x})$ . We generate  $u$  by using smooth functions  $\hat{\mathbf{u}}(x, y, z)$  parameterized in the embedding space  $\mathbb{R}^3$ . By the smoothness of the surface manifolds  $\mathcal{M}$ , evaluation at  $\mathbf{x} \in \mathcal{M}$  gives a smooth surface field  $u$ . More formally, this corresponds to using the inclusion map  $\iota: \mathbb{R}^3 \hookrightarrow \mathcal{M}$  to obtain  $\mathbf{u}(\mathbf{x}) = \iota_{\mathbf{x}}\hat{\mathbf{u}}(\cdot)$ . We also use this inclusion map approach to generate test surface drift tensors  $\mathbf{a}$  and diffusion tensors  $\mathbf{b}$  for the stochastic process  $\mathbf{X}_t$  arising in equation 2 and 5.

For our validation studies, we generate test fields  $u$  for the Manifolds A–D using  $\mathbf{u}(\mathbf{x}) = z(x^4 + y^4 - 6x^2y^2)$ , which is an extension of a degree 5 Spherical Harmonic to  $\mathbb{R}^3$ . For the drift-diffusion tensors for Manifold A, we use

$$\mathbf{a}_A = y\tilde{\sigma}_1 + xz\tilde{\sigma}_1, \quad \mathbf{b}_A = [xz\tilde{\sigma}_1 + y^2\tilde{\sigma}_2, xyz\tilde{\sigma}_1 + \cos(y^2)\tilde{\sigma}_2, z\tilde{\sigma}_1 + (y^3 + x)\tilde{\sigma}_2]. \quad (20)$$

The  $\tilde{\sigma}_1, \tilde{\sigma}_2$  provide a local orthogonal tangent basis at every point on the Manifold A. In practice in our numerical calculations, this does not need to be smooth in  $\mathbf{x}$  and we construct these as convenient using our local tangent plane approximation and Gram-Schmidt orthogonalization [23].

For the Manifolds B and C, we use for the drift-diffusion tensors tangential projections of the vector fields in  $\mathbb{R}^3$  given by

$$\mathbf{a}_{B,C} = [y, xz, x^2yz]^T, \quad \mathbf{b}_{B,C} = [(xz, xyz, z), (y^2, \cos(y^2), y^3 + x), (x^2 + y, e^{-z}, e^y)]^T. \quad (21)$$

For Manifold D, we use drift-diffusion tensors

$$\mathbf{a}_D = y\sigma_u + xz\sigma_v, \quad \mathbf{b}_D = [\sin(xy)\sigma_u + y^2\sigma_v, xyz\sigma_u + \cos(y^2)\sigma_v, e^z\sigma_u + (y^3 + x)\sigma_v]. \quad (22)$$

The  $\sigma_u, \sigma_v$  provide a basis for the tangent space smooth in  $\mathbf{x}$  given by the directional derivatives of the global parameterization  $\sigma(u, v)$  of the torus [14]. We characterize the accuracy of the GMLS approximation  $\tilde{L}$  of the surface operators  $\mathcal{L}$  using the  $\ell^2$ -error

$$\epsilon_{op}^2(\tilde{L}) = \left\| \tilde{L}u - \mathcal{L}u \right\|_{n,2}^2 = \frac{1}{n} \sum_{i=1}^n \left( \tilde{L}u(\mathbf{x}_i) - \mathcal{L}u(\mathbf{x}_i) \right)^2. \quad (23)$$

In these studies, we evaluate to high precision the action of the operators  $\mathcal{L}$  by symbolic calculations using SymPy [44]. In general, we emphasize that such calculations of expressions symbolically can be prohibitive. Using this approach, we investigate the accuracy of the GMLS approximation of the operator for each of the manifolds and with approximation spaces with multivariate polynomials of degree  $m \in \{2, 4, 6\}$ . These results are reported in Tables 1–3.

### 3.3. Results of Convergence Studies

We performed convergence studies for the Manifolds A–D shapes in Figure 3 with the test fields  $u$  and drift-diffusion tensors  $\mathbf{a}, \mathbf{b}$  discussed in Section 3.2. As the manifold resolution is refined, we study the convergence of the GMLS approximations of the surface operators using for spaces  $\mathbb{V}$  multivariate polynomials of degree  $m \in \{2, 4, 6\}$ . We estimate the convergence rates using the log-log slope of the error  $\epsilon_{op}$  as the fill distance parameter  $h$  is varied between levels of refinement. We report these results in Tables 1–3.

We find in our empirical results that when using GMLS with polynomial spaces of degree  $m$  to evaluate the elliptic PDEs operator  $\mathcal{L}$  of order  $k$ , we obtain convergence results of order  $m$ . We remark that there is no theory for our surface operators, since there is a non-linearity from the coupling between the surface geometry and the operator differential terms. Our results are suggestive that our surface operator approximations achieve results exhibiting a trend consistent with simpler differential operators approximated by GMLS [25]. This suggests our methods are resolving the surface geometric contributions with sufficient precision to minimize their contributions to the error. Since the operator  $\mathcal{L}$  is of differential order  $k = 2$  we use throughout approximating polynomial spaces of at least degree  $m \geq k \geq 2$ .

h	Manifold A		Manifold B		Manifold C		h	Manifold D	
	$\ell_2$ -error	Rate	$\ell_2$ -error	Rate	$\ell_2$ -error	Rate		$\ell_2$ -error	Rate
0.1	2.6503e-02	-	3.6072e-02	-	1.1513e-02	-	.08	8.1920e-03	-
0.05	5.8961e-03	2.14	8.3322e-03	2.11	2.3778e-03	2.27	.04	1.8071e-03	2.21
0.025	1.4951e-03	1.97	2.1451e-03	1.95	6.3865e-04	1.90	.02	4.3928e-04	2.06
0.0125	3.5399e-04	2.07	5.1159e-04	2.06	1.6225e-04	1.98	.01	1.0461e-04	2.05

**Table 1.:** GMLS Convergence Rates for  $\mathcal{L}$ . For our GMLS methods using approximation spaces based on multivariate polynomials of degree  $m = 2$ , we find convergence rate of  $\sim 2^{nd}$  order.

h	Manifold A		Manifold B		Manifold C		h	Manifold D	
	$\ell_2$ -error	Rate	$\ell_2$ -error	Rate	$\ell_2$ -error	Rate		$\ell_2$ -error	Rate
0.1	5.8394e-03	-	2.5843e-02	-	5.5971e-03	-	.08	2.5936e-03	-
0.05	2.0355e-04	4.78	1.1594e-03	4.48	3.7890e-04	3.88	.04	1.0359e-04	4.72
0.025	1.1382e-05	4.14	8.2945e-05	3.80	1.9628e-05	4.27	.02	5.4028e-06	4.30
0.0125	6.6746e-07	4.08	5.1207e-06	4.01	1.4226e-06	3.79	.01	3.0733e-07	4.11

**Table 2.:** GMLS Convergence Rates for  $\mathcal{L}$ . For our GMLS methods using approximation spaces based on multivariate polynomials of degree  $m = 4$ , we find convergence rate of  $\sim 4^{th}$  order.

h	Manifold A		Manifold B		Manifold C		h	Manifold D	
	$\ell_2$ -error	Rate	$\ell_2$ -error	Rate	$\ell_2$ -error	Rate		$\ell_2$ -error	Rate
0.1	1.8032e-05	-	2.0087e-03	-	2.1854e-03	-	.08	2.7306e-04	-
0.05	2.3775e-07	6.16	5.4584e-05	5.21	1.1625e-04	4.24	.04	2.6141e-06	6.81
0.025	4.3492e-09	5.75	1.4770e-06	5.20	1.5943e-06	6.20	.02	7.4551e-08	5.18
0.0125	6.4443e-11	6.06	1.9655e-08	6.22	3.1347e-08	5.68	.01	1.6423e-09	5.47

**Table 3.:** *GMLS Convergence Rates for  $\mathcal{L}$ . For our GMLS methods using approximation spaces based on multivariate polynomials of degree  $m = 6$ , we find convergence rate of  $\sim 6^{\text{th}}$  order.*

## 4. Results for First Passage Times on Surfaces

For first passage times on surfaces, we investigate the roles played by the geometry, drift dynamics, and spatial-dependence of diffusivity. For our studies, we consider the general surface Langevin dynamics

$$d\mathbf{X}_t = -\frac{1}{\gamma}\nabla_{\mathbf{X}}U(\mathbf{X})dt + \sqrt{2D}\mathbf{I}d\mathbf{W}_t \quad (24)$$

subject to  $\mathbf{X}_t \in \mathcal{M}$ .

The dynamics are expressed here in the embedding space  $\mathbf{X}_t \in \mathbb{R}^3$  and constrained to be within the manifold surface  $\mathcal{M}$ . We could also express these dynamics using local coordinate charts on the surface as discussed in Section 1.1. The  $U$  is the potential energy,  $\gamma$  the friction coefficient,  $D = K_B T / \gamma$  the diffusivity, and  $K_B T$  the thermal energy with  $K_B$  the Boltzmann constant and  $T$  the temperature [9]. In terms of the drift-diffusion tensors,  $\mathbf{a}(\mathbf{X}_t) = \gamma^{-1}\nabla_{\mathbf{X}}U(\mathbf{X})$ ,  $\mathbf{b}(\mathbf{X}_t) = \sqrt{2D}\mathbf{I}$ .

### 4.1. Role of Drift in Mean First Passage Times: Double Well Potential

Using our methods to capture drift in the surface dynamics, we study the role that can be played by surface potentials in influencing stochastic trajectories and the first passage time. We consider the case of a double-well potential  $U$  on a surface which from the conservative force  $F = -\nabla_X U$  in equation 24 introduces a drift into the dynamics influencing the mean first passage time. We consider geometries  $\Omega$  described by the truncated torus, parameterized by

$$\mathbf{X}(u, v) = [\cos(u)(.7 + .3 \cos(v)), \sin(u)(.7 + .3 \cos(v)), .3 \sin(v)]^T, \quad u \in \left[\frac{\pi}{4}, \frac{7\pi}{4}\right], \quad v \in [0, 2\pi).$$

The double-well potential  $U$  is generated using the parameterization  $(u, v)$  as

$$U(\mathbf{x}) = k \sin^2(u); \quad \mathbf{x} = \mathbf{X}(u, v). \quad (25)$$

We study how the mean first passage time changes as we vary the energy barrier  $k = \tilde{k} \cdot k_B T$  with  $\tilde{k} \in \{0.0, 0.05, 0.1, 0.5, 1.0, 2.0, 5.0\}$ . The case  $\tilde{k} = 0.0$  serves as our baseline case with no drift. The energy minimum occurs at  $u = \pi$  and has energy barriers at  $u = \pi/2$  and  $u = 3\pi/2$  near the

boundaries at  $u = \pi/4$  and  $u = 7\pi/4$ . We report the results of the first passage times starting at the specific locations  $X_i$  given by

$$\begin{aligned} \mathbf{X}_0 : (u, v) &= (\pi, 0) & \mathbf{X}_1 : (u, v) &= \left(\pi, \frac{\pi}{2}\right) & \mathbf{X}_2 : (u, v) &= (\pi, \pi) \\ \mathbf{X}_3 : (u, v) &= \left(\frac{\pi}{2}, 0\right) & \mathbf{X}_4 : (u, v) &= \left(\frac{\pi}{2}, \frac{\pi}{2}\right) & \mathbf{X}_5 : (u, v) &= \left(\frac{\pi}{2}, \pi\right) \\ \mathbf{X}_6 : (u, v) &= \left(\frac{\pi}{3}, 0\right) & \mathbf{X}_7 : (u, v) &= \left(\frac{\pi}{3}, \frac{\pi}{2}\right) & \mathbf{X}_8 : (u, v) &= \left(\frac{\pi}{3}, \pi\right). \end{aligned}$$

We report our results in Figure 4.

In our studies the starting locations  $X_0, X_1, X_2$  are at the minimum of the potential energy  $U$ . From these locations each trajectory must surmount at least one of the energy barriers to reach the boundary. This results in the largest first passage times. We find as the energy barrier is increased  $k \gtrsim k_B T$  there is approximately exponential increase in the first passage times. This is in agreement with theory for first passage times involving energy barriers based on asymptotic analysis using Kramer's approximation [4]. Our numerical methods allow for computing the full solution  $u(\mathbf{x})$  of equation 3, including first passage times, over a wide range of regimes  $k \ll k_B T$ ,  $k \sim k_B T$ , and  $k \gg k_B T$ , and when starting at locations that are not only at the potential energy minimum, see Figure 4.

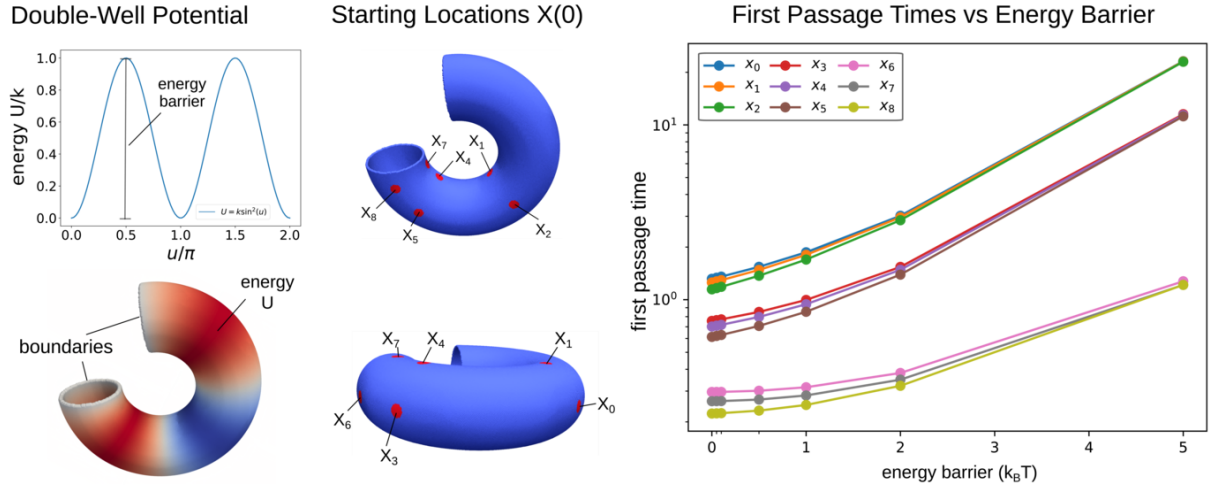


**Figure 4.:** (left) Double-well potential  $U$  on the surface of equation 25 influencing the drift of the stochastic dynamics in 24. (middle) The starting locations for first passage times with  $\mathbf{X}(0) = \mathbf{X}_i$ . (right) First passage times from the selected starting points as the strength of the energy barrier  $k$  of the double-well potential is varied. The locations  $X_0, X_1, X_2$  start at the minimum of the potential energy and exhibit the longest first passage times since they must surmount at least one of the energy barriers to reach the boundary. As the energy barrier is increased the first passage times increase, most rapidly when  $k \gtrsim k_B T$ , and with an exponential trend in agreement with Kramer's theory [4].

## 4.2. Role of Diffusion in Mean First Passage Times: Spatially-Dependent Diffusivities

We study the role of spatially-dependent heterogeneous diffusivities  $b = b(\mathbf{X})$  in first passage times. We consider the surface geometry  $\Omega$  obtained from the truncated torus

$$\mathbf{X}(u, v) = [0.4 \sin(v), \sin(u)(1 + 0.4 \cos(v)), -\cos(u)(1 + 0.4 \cos(v))]^T, \quad u \in \mathcal{U}(z = 0, v), v \in [0, 2\pi).$$

This geometry is obtained by slicing the torus at  $z = 0$ . This defines the boundary  $\partial\Omega$  and for the parameterization  $(u, v)$  a range  $\mathcal{U}$  for  $u$  that depends on each value of  $v$ . We consider the spatially-dependent diffusivity

$$\mathbf{b}(\mathbf{x}) = \sqrt{2D(\mathbf{x})}\mathbf{I} = \sqrt{2D_0} \left( 1 - c \exp\left(\frac{-\|\mathbf{x} - \mathbf{x}_c\|^2}{r^2}\right) \right) \mathbf{I}, \quad (26)$$

$$\mathbf{x}_c : (u_c, v_c) = \left(\frac{3\pi}{4}, \frac{\pi}{2}\right), \quad r \geq 0, 0 \leq c < 1. \quad (27)$$

This corresponds in equation 24 to  $D = D(\mathbf{x}), \gamma = \gamma(\mathbf{x})$ , and zero drift with  $U = 0$  so  $\mathbf{a}(\mathbf{x}) = 0$ . The exponential is centered at  $\mathbf{x}_c$  with decay over length-scale  $r$  and influence amplitude  $c$ . For  $r$  sufficiently small the variations in diffusivity will occur primarily inside the domain  $\Omega$  in a localized region  $\|\mathbf{x} - \mathbf{x}_c\| \lesssim 3r$ . The diffusivity elsewhere will be approximately constant  $\sim D$ . We consider for our initial starting locations

$$\begin{aligned} \mathbf{X}_0 : (u, v) &= (\pi, 0) & \mathbf{X}_1 : (u, v) &= \left(\pi, \frac{\pi}{2}\right) & \mathbf{X}_2 : (u, v) &= (\pi, \pi) \\ \mathbf{X}_3 : (u, v) &= \left(\frac{3\pi}{4}, 0\right) & \mathbf{X}_4 : (u, v) &= \left(\frac{3\pi}{4}, \frac{\pi}{2}\right) & \mathbf{X}_5 : (u, v) &= \left(\frac{3\pi}{4}, \pi\right) \\ \mathbf{X}_6 : (u, v) &= \left(\frac{5\pi}{4}, 0\right) & \mathbf{X}_7 : (u, v) &= \left(\frac{5\pi}{4}, \frac{\pi}{2}\right) & \mathbf{X}_8 : (u, v) &= \left(\frac{5\pi}{4}, \pi\right). \end{aligned}$$

We study the role of spatially-dependent diffusivity in two cases: (i) when the depth  $c$  is varied while leaving the area scale  $r$  fixed, and (ii) when the area scale  $r$  is varied while leaving the depth  $c$  fixed. We use throughout the baseline parameters  $c = 0.9$  and  $r = 0.5$ . We show the geometry and solution for a typical spatially dependent diffusivity in Figure 5. We report our results in Figure 6.

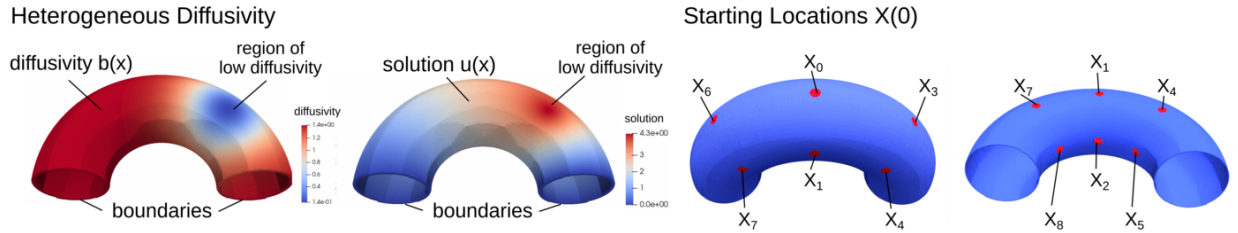


**Figure 5.:** *Spatially Dependence Diffusivities.* (left) The heterogeneous spatially dependent diffusivity  $b(\mathbf{x})$  in equation 26. (left-middle) The solution  $u(\mathbf{x})$  for the first passage time problem of equation 6. (right-middle), (right) The starting locations  $\mathbf{X}(0) = \mathbf{X}_i$ . We report results of studies in Figure 6.

We find varying the spatial extent  $r$  of the diffusivity plays a particularly strong role in the first passage times. The underlying mechanisms are different than the double-well potential. When

a trajectory approaches  $\mathbf{x}_c$  the motion of the stochastic process slows down significantly as a result of the smaller diffusivity. There is no barrier for  $\mathbf{X}_t$  to approach such regions but once within this region exhibits a type of temporary trapping behavior from the slow diffusion. We see from Figure 5, such a region influences the first passage time over a much larger range than the direct variations in  $b(\mathbf{x})$  given the high probability of a large fraction of trajectories encountering this trapping region even when a modest distance away. We see increases in  $r$  have a strong influence on increasing the first passage times, see Figure 6. We also see in the limit that the localized diffusivity  $b(\mathbf{x})$  approaches zero, even a relatively small probability of encountering this region can result in a large first passage time. We see this increasing influence as  $c$  approaches one, see Figure 6.

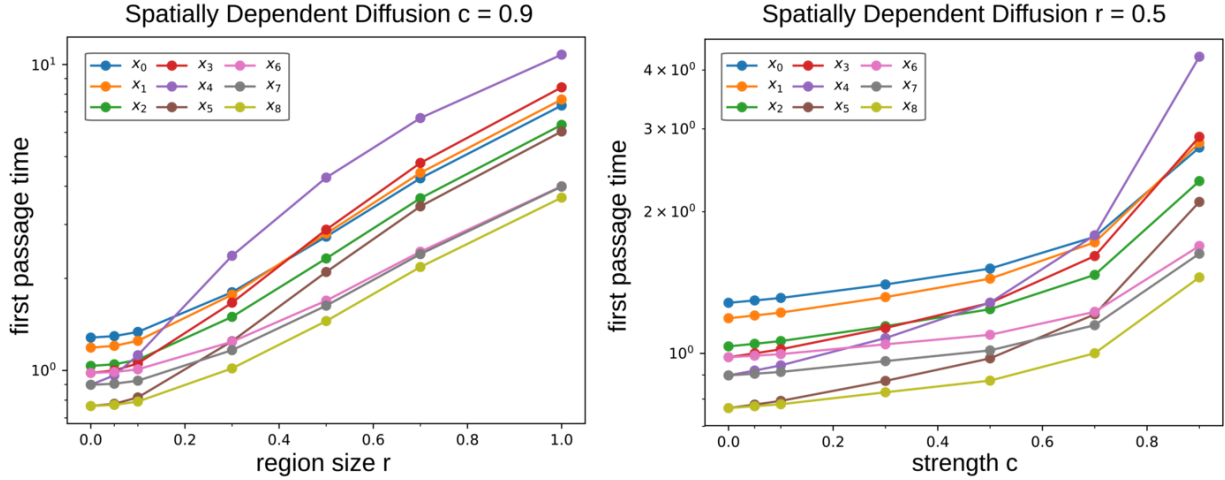


**Figure 6.:** *Spatially Dependent Diffusivity and First Passage Times.* (left) The first passage times for the spatially dependent diffusivity  $b(\mathbf{x})$  in equation 26 when varying the size  $r$  of the region of low diffusivity. (right) The first passage times when increasing the strength  $c$  of the diffusivity reduction in equation 26.

### 4.3. Role of Geometry in Mean First Passage Times: Neck-Shaped Domains

We show how our methods can be used to investigate how the shape of the manifold surface influences first passage times. In these studies, we consider purely diffusive dynamics. This corresponds to the case with  $U = 0$  with zero drift  $\mathbf{a}(\mathbf{x}) = 0$  and a spatially homogeneous diffusivity  $\mathbf{b}(\mathbf{x}) = \sqrt{2D_0}I$  in equation 24. For the geometry we use a surface of revolution with an adjustable shape that forms a neck region near the bottom at  $z = 0$ , see Figure 7. This geometry is generated by considering first a cylinder of radius  $r_0$  and height  $h = 0.05$  which is capped at the top by a sphere. We then use a radial profile  $r(z)$  to connect the spherical cap with the bottom of the cylinder of radius  $r_0$  at  $z = 0$ . For this purpose, we use a bump function  $r(z) = (1 - 0.4b) + 0.4b \exp\left(1 - \frac{b^2}{b^2 - b + .05 - z^2}\right)$ . For  $z \in [0.05, b + 0.05]$ , we choose  $b$  so that this has arc-length  $\pi/2$ , and the final radius  $r_0$  at  $z = 0$ . This serves to smoothly connect the unit hemisphere cap to the bottom of the cylinder with radius  $r_0$ . This ensures the geodesic distance from  $X(0) = X_i$  to the boundary is always the same as we vary the shapes, see Figure 7. We report our results in Figure 8.

We find as the neck region becomes smaller it acts as a hindrance for trajectories to reach the boundary and first passage times increase. From the log-log plot we see that the first passage

time appears over many radii to follow a power-law trend  $\bar{\tau} \sim r^\alpha$  with values for  $\alpha$  respectively for  $X(0) = X_0, X_1, X_2$  having  $\alpha \approx 0.427, 0.484, 0.893$ . As the radius tends to 0 we see the first passage time diverges. We see for points further from the boundary the first passage times are longer as would be expected. However, as the neck region becomes small, we see smaller differences occur between points  $X_0, X_1$  starting at points above the neck region, compared to the point  $X_3$  starting within the neck region. This indicates that as the radius shrinks the neck region increasingly acts as a hindrance for reaching the boundary. Interesting, we also see that starting at  $X_3$  also has FPTs that significantly increase, since as  $r_0 \rightarrow 0$  an increasingly large fraction of trajectories will leave the neck region before encountering the boundary and then must also overcome the hindrance similar to starting at  $X_0, X_1$ . We can characterize this mechanism by using a reaction-coordinate and notion of free energy (entropy contributions) arising from the constricting geometry.

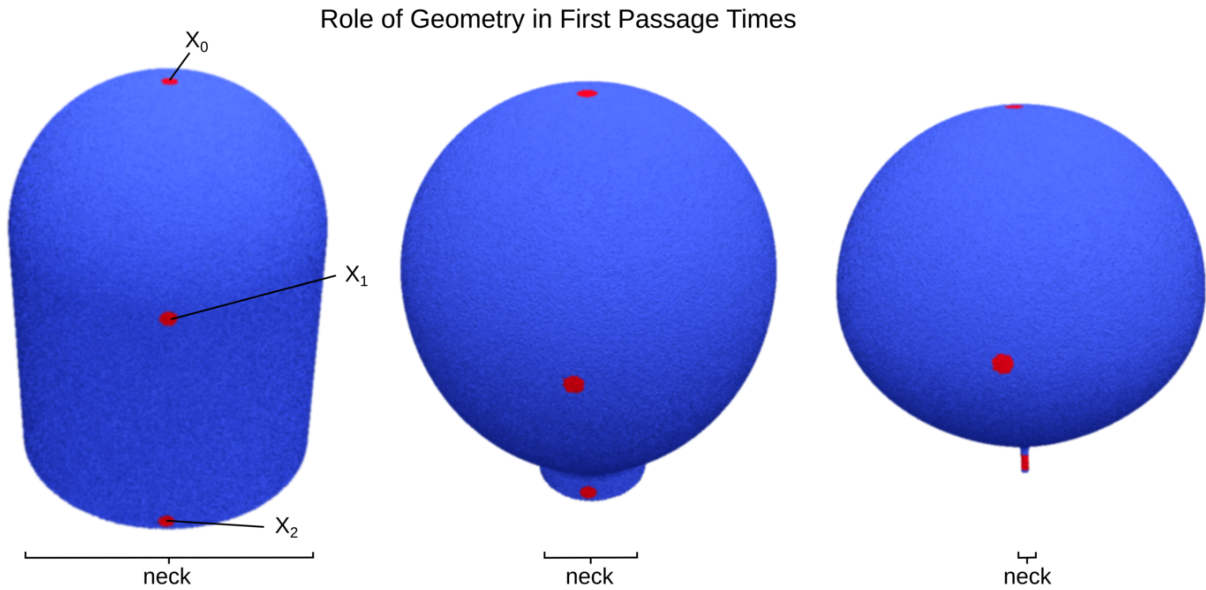


**Figure 7.:** For the FPT studies when varying the geometry of the neck region, we show the select starting locations  $\mathbf{X}(0) = \mathbf{X}_i$  (red points). On the left we show the largest neck domain which does not present a geometric bottleneck for reaching  $z = 0$ . On the right, we show the smallest neck region which presents a significant geometric bottleneck potentially inhibiting diffusion in reaching  $z = 0$ . The geometries used in these studies were designed so that as the neck width is varied the geodesic distance from the starting points remains constant to reach the boundary at  $z = 0$ .

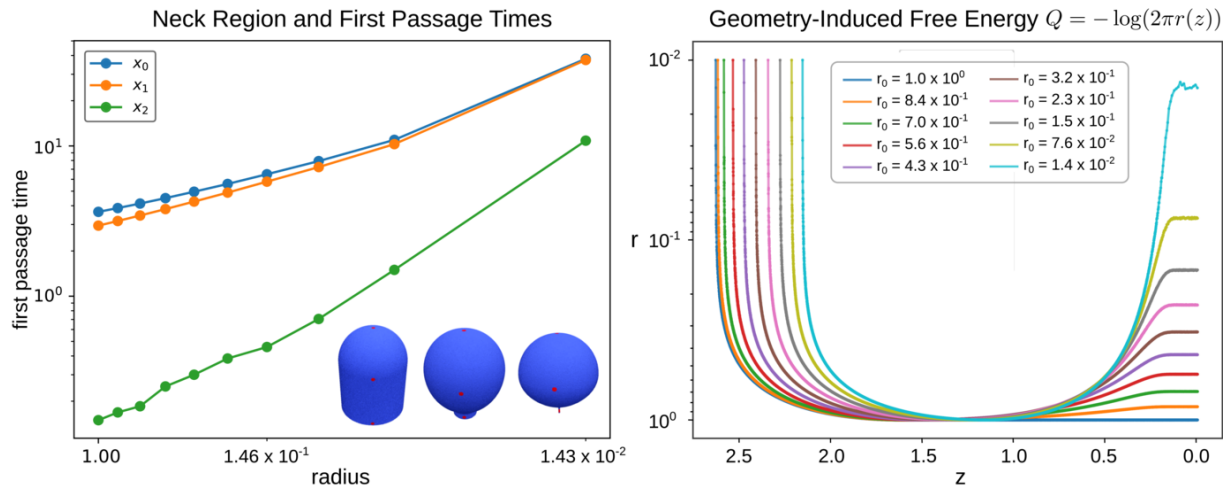


**Figure 8.:** (left) The first passage time as the neck radius  $r$  becomes small. We see as the neck becomes narrower (towards the right) the geometry of the manifold restricts the diffusion and reaching the boundary becomes more difficult. The  $r$  indicates the narrowest radius of the shape. (right) The shape acts to give a geometrically induced free energy  $Q(z) = -\log(2\pi r(z))$  for the dynamics when projecting to the  $z$ -axis. We see as the neck radius  $r$  narrows (towards the right) the geometry creates an increasingly large free-energy barrier and increases the first-passage times.

Given the radial symmetry we can project the stochastic dynamics onto the  $z$ -component as an effective reaction-coordinate for reaching the boundary at  $z = 0$ . This provides a statistical mechanics model [9] where the shape of the manifold gives an effective free energy having entropic contributions proportional to  $Q(z) = -\log(2\pi r(z))$ . This contributes to an effective mean-force for  $Z_t$  yielding the drift  $a(z) = -\partial Q/\partial z = -Q'(z)$ . This suggests the radially-averaged stochastic dynamics  $dZ_t = -Q'(Z_t)dt + C dW_t$ . From this perspective, the drift-diffusion process  $Z_t$  must cross the geometrically-induced energy barrier  $Q(z)$  to reach the boundary at  $z = 0$ . Similar to our results on double-well potentials, this could be studied analytically with asymptotic Kramer's theory [4]. Our numerical methods allow for capturing directly these effects and we see as the neck narrows this significantly increases the first passage times. This correlates well with how the effective free energy barrier for  $Z_t$  increases with the shape change, see Figure 8. Our results show how geometric effects captured by our methods can provide mechanisms that influence significantly the behaviors of stochastic processes and their first passage times.

## Conclusions

We have developed computational methods based on Generalized Moving Least Squares (GMLS) for investigating first passage times on surfaces of general shape and topology. We showed for a variety of shapes that our methods converge with high-order accuracy both in capturing the geometry and the PDE solutions. We showed how our methods could be used to investigate how statistics are influenced by the surface geometry, drift dynamics, and spatially dependent diffusivities. The solvers we have developed can be used more generally also for computing other path-dependent statistics and solutions to elliptic boundary-value problems on surfaces of general shape.



## Acknowledgements

The authors would like to acknowledge support from research grants DOE ASCR PhILMS DE-SC0019246 and NSF DMS-1616353.

## Appendix

### A. Generalizing Vector Calculus to Manifolds using Exterior Calculus

Many of the operators used in vector calculus can be generalized naturally to the manifold setting. For this purpose, we utilize the operators of exterior calculus given by the Hodge star  $\star$ , exterior derivative  $\mathbf{d}$ , and vector to co-vector isomorphisms  $\flat, \sharp$  (definitions below) [5]. We denote vector fields and tensors using the notation  $\mathbf{a} = a^{i_1 \dots i_k} \partial_{i_1} \dots \partial_{i_k}$ . We use  $\partial_{i_k}$  to denote the basis vector  $\partial_{i_k} = \partial \sigma / \partial x^{i_k}$  and tensor product these together to represent vectors and tensors for the choice of coordinates  $\mathbf{x} = (x^1, x^2, \dots, x^d)$ . We denote a differential  $k$ -form as  $\alpha = (1/k!) \alpha_{i_1, \dots, i_k} \mathbf{d}\mathbf{x}^{i_1} \wedge \dots \wedge \mathbf{d}\mathbf{x}^{i_k}$ . The  $\wedge$  denotes the wedge-product of a tensor. We use the convention here with  $1/k!$  to allow summations over all permutations of the index values for  $i_1, \dots, i_k$ . A more detailed discussion of tensor calculus on manifolds can be found in [5].

We formulate the generalized operators in terms of the co-vectors (differential forms)  $f^\flat$  and  $\mathbf{F}^\flat$ . We use that in the case of a scalar field we have quantitatively at each point  $f = f^\flat$ . The isomorphisms  $\flat, \sharp$  mapping between the vector and co-vector spaces are given by

$$\mathbf{a}^\flat = (1/k!) g_{i_1, \ell_1} \dots g_{i_k, \ell_k} a^{\ell_1 \dots \ell_k} \mathbf{d}\mathbf{x}^{i_1} \wedge \dots \wedge \mathbf{d}\mathbf{x}^{i_k} \quad (28)$$

$$\alpha^\sharp = (1/k!) g^{i_1, \ell_1} \dots g^{i_k, \ell_k} \alpha_{\ell_1 \dots \ell_k} \partial_{\mathbf{x}^{i_1}} \dots \partial_{\mathbf{x}^{i_k}}. \quad (29)$$

The exterior derivative  $\mathbf{d}$  of a differential  $k$ -form  $\alpha$  is defined in terms of the coordinates  $\mathbf{x}$  as

$$\mathbf{d}\alpha = \frac{1}{k!} \frac{\partial}{\partial x^j} \alpha_{i_1, \dots, i_k} \mathbf{d}\mathbf{x}^j \wedge \mathbf{d}\mathbf{x}^{i_1} \wedge \dots \wedge \mathbf{d}\mathbf{x}^{i_k}. \quad (30)$$

The Hodge star  $\star$  is defined in terms of the coordinates  $\mathbf{x}$  as

$$\star \alpha = \frac{\sqrt{|g|}}{(n-k)!k!} \alpha^{i_1, \dots, i_k} \epsilon_{i_1, \dots, i_k, j_1, \dots, j_{n-k}} \mathbf{d}\mathbf{x}^{j_1} \wedge \dots \wedge \mathbf{d}\mathbf{x}^{j_{n-k}}. \quad (31)$$

Note the indices have been raised here for the  $k$ -form with  $\alpha^{i_1, \dots, i_k} = g^{i_1 \ell_1} \dots g^{i_k \ell_k} \alpha_{\ell_1, \dots, \ell_k}$ . The  $\epsilon_{\ell_1, \dots, \ell_n}$  denotes the Levi-Civita tensor which gives the sign of the permutation of the indices  $\ell_1, \dots, \ell_n$  and is otherwise zero [5].

We can also generalize operators of vector calculus in the context of manifolds acting on scalar fields  $f$  and vector fields  $\mathbf{F}$  as

$$\begin{aligned} \text{grad}_{\mathcal{M}}(f) &= [\mathbf{d}f]^\sharp, & \text{div}_{\mathcal{M}}(\mathbf{F}) &= -(-\star \mathbf{d} \star \mathbf{F}^\flat) = -\delta \mathbf{F}^\flat, \\ \text{curl}_{\mathcal{M}}(\mathbf{F}) &= -\star \mathbf{d} [\mathbf{F}^\flat], & \text{curl}_{\mathcal{M}}(f) &= [-\star \mathbf{d}f]^\sharp. \end{aligned} \quad (32)$$

We define  $\delta = (-\star \mathbf{d} \star)$  which is referred to as the co-differential. To define  $\mathbf{d}$  the exterior derivative and  $\star$  the Hodge star, we consider the tangent bundle  $\mathcal{TM}$  of the manifold and its dual co-tangent

bundle  $\mathcal{TM}^*$ . The tangent bundle defines the spaces for scalar fields, vector fields, and more generally rank  $m$  tensor fields over the manifold. The co-tangent bundle is the space of duals to these fields. The co-tangent bundle can be viewed as the space of differential forms of order 0, 1, and  $m$ . More details on the associated differential geometry can be found in [5, 11, 14]. Additional information on our approaches for using these operators can be found in [39, 41, 48].

## B. Exterior Calculus Operators Expressed in Coordinates

We use as conventions that for differential 0-forms (scalar functions)  $f_j = \partial_{x^j} f$ , for differential 1-forms (co-vector fields)  $\alpha = \alpha_j \mathbf{d}x^j$ , and for vector fields  $\mathbf{v} = v^j \partial_j$ . In each case we have  $j \in \{u, v\}$ . The isomorphisms  $\sharp$  and  $\flat$  between vectors and co-vectors can be expressed explicitly as

$$\begin{aligned} \mathbf{v}^\flat &= (v^u \boldsymbol{\sigma}_u + v^v \boldsymbol{\sigma}_v)^\flat & (33) \\ &= v^u g_{uu} \mathbf{d}u + v^u g_{uv} \mathbf{d}v + v^v g_{vu} \mathbf{d}u + v^v g_{vv} \mathbf{d}v \\ &= (v^u g_{uu} + v^v g_{vu}) \mathbf{d}u + (v^u g_{uv} + v^v g_{vv}) \mathbf{d}v \end{aligned}$$

$$\begin{aligned} (\alpha)^\sharp &= (\alpha_u \mathbf{d}u + \alpha_v \mathbf{d}v)^\sharp & (34) \\ &= \alpha_u g^{uu} \boldsymbol{\sigma}_u + \alpha_u g^{uv} \boldsymbol{\sigma}_v + \alpha_v g^{vu} \boldsymbol{\sigma}_u + \alpha_v g^{vv} \boldsymbol{\sigma}_v \\ &= (\alpha_u g^{uu} + \alpha_v g^{vu}) \boldsymbol{\sigma}_u + (\alpha_u g^{uv} + \alpha_v g^{vv}) \boldsymbol{\sigma}_v. \end{aligned}$$

We use the conventions for the notation that for the embedding map  $\boldsymbol{\sigma}$  we have  $\boldsymbol{\sigma}_u = \partial_u$  and  $\boldsymbol{\sigma}_v = \partial_v$  as in Appendix C. The exterior derivatives on these  $k$ -forms can be expressed as

$$\mathbf{d}f = (\partial_u f) \mathbf{d}u + (\partial_v f) \mathbf{d}v = f_u \mathbf{d}u + f_v \mathbf{d}v \quad (35)$$

$$\mathbf{d}\alpha = (\partial_u \alpha_v - \partial_v \alpha_u) \mathbf{d}u \wedge \mathbf{d}v. \quad (36)$$

The generalized curl of a 0-form and 1-form can be expressed in coordinates as

$$-\star \mathbf{d}f = \sqrt{|g|} (f_u g^{uv} + f_v g^{vv}) \mathbf{d}u - \sqrt{|g|} (f_u g^{uu} + f_v g^{vu}) \mathbf{d}v \quad (37)$$

$$-\star \mathbf{d}\alpha = \frac{\partial_v \alpha_u - \partial_u \alpha_v}{\sqrt{|g|}}. \quad (38)$$

A further discussions of these operators of differential geometry can be found in [5, 11, 14]. Additional details on our approach can be found in [39, 41, 48].

## C. Monge-Gauge Surface Parameterization

In the Monge-Gauge we parameterize locally a smooth surface in terms of the tangent plane coordinates  $u, v$  and the height of the surface above this point as the function  $h(u, v)$ . This gives the embedding map

$$\mathbf{x}(u, v) = \boldsymbol{\sigma}(u, v) = (u, v, \mathbf{h}(u, v)). \quad (39)$$

We can use the Monge-Gauge equation 39 to derive explicit expressions for geometric quantities. The derivatives of  $\boldsymbol{\sigma}$  provide a basis  $\partial_u, \partial_v$  for the tangent space as

$$\partial_u = \boldsymbol{\sigma}_u(u, v) = (1, 0, \mathbf{h}_u(u, v)) \quad (40)$$

$$\partial_v = \boldsymbol{\sigma}_v(u, v) = (0, 1, \mathbf{h}_v(u, v)). \quad (41)$$

The first fundamental form  $\mathbf{I}$  (metric tensor) and its inverse  $\mathbf{I}^{-1}$  (inverse tensor) are given by

$$\mathbf{I} = \begin{bmatrix} g_{uu} & g_{uv} \\ g_{vu} & g_{vv} \end{bmatrix} = \begin{bmatrix} \boldsymbol{\sigma}_u \cdot \boldsymbol{\sigma}_u & \boldsymbol{\sigma}_u \cdot \boldsymbol{\sigma}_v \\ \boldsymbol{\sigma}_v \cdot \boldsymbol{\sigma}_u & \boldsymbol{\sigma}_v \cdot \boldsymbol{\sigma}_v \end{bmatrix} = \begin{bmatrix} 1 + \mathbf{h}_u(u, v)^2 & \mathbf{h}_u \mathbf{h}_v(u, v) \\ \mathbf{h}_u(u, v) \mathbf{h}_v(u, v) & 1 + \mathbf{h}_v(u, v)^2 \end{bmatrix}. \quad (42)$$

and

$$\mathbf{I}^{-1} = \begin{bmatrix} g^{uu} & g^{uv} \\ g^{vu} & g^{vv} \end{bmatrix} = \frac{1}{1 + \mathbf{h}_u^2 + \mathbf{h}_v^2} \begin{bmatrix} 1 + \mathbf{h}_v^2 & -\mathbf{h}_u \mathbf{h}_v \\ -\mathbf{h}_u \mathbf{h}_v & 1 + \mathbf{h}_u^2 \end{bmatrix}. \quad (43)$$

We use throughout the notation for the metric tensor  $\mathbf{g} = \mathbf{I}$  interchangeably. For notational convenience, we use the tensor notation for the metric tensor  $g_{ij}$  and for its inverse  $g^{ij}$ . These correspond to the first fundamental form and its inverse as

$$g_{ij} = [\mathbf{I}]_{i,j}, \quad g^{ij} = [\mathbf{I}^{-1}]_{i,j}. \quad (44)$$

For the metric tensor  $\mathbf{g}$ , we also use the notation  $|g| = \det(\mathbf{g})$  and have that

$$\sqrt{|g|} = \sqrt{\det(\mathbf{I})} = \sqrt{1 + \mathbf{h}_u^2 + \mathbf{h}_v^2} = \|\vec{\sigma}_u(u, v) \times \vec{\sigma}_v(u, v)\|. \quad (45)$$

This provides the local area element as  $dA_{u,v} = \sqrt{|g|} du dv$ . Lastly, we must compute the Christoffel symbols of the second kind in our derivation of drift-diffusion on manifolds. In the general case this is given by

$$\Gamma_{ij}^k = \partial_j \boldsymbol{\sigma}_i \cdot \boldsymbol{\sigma}_k. \quad (46)$$

This can become complicated in general coordinates. However, in the case of the Monge Patch the above simplifies to

$$\Gamma_{ij}^k = \frac{\mathbf{h}_{ij} \mathbf{h}_k}{\sqrt{|g|}} = \frac{\mathbf{h}_{ij} \mathbf{h}_k}{\sqrt{1 + \mathbf{h}_u^2 + \mathbf{h}_v^2}}. \quad (47)$$

For further discussions of these tensors and more generally the differential geometry of manifolds see [5, 11, 14]. We use these expressions as the basis of our calculations of the action of our surface operators.

## D. Sampling Resolution of the Manifolds

We provide a summary of the sampling resolution  $h$  used for each of the manifolds in Table 4. We refer to  $h$  as the *target fill distance*. For each of the manifolds and target spacing  $h$ , we achieve a nearly uniform collection of the points (quasi-uniform samplings) using DistMesh [16]. In practice, we have found this yields a point spacing with neighbor distances varying by about  $\approx \pm 30\%$  relative to the target distance  $h$ . We summarize for each of the manifolds how this relates to the number of sample points  $n$  in Table 4. Robustness studies for related solvers have been carried out when applying perturbations to such point samples in [52].

Refinement Level	A: h	n	B: h	n	C: h	n	D: h	n
1	.1	2350	.1	2306	.1	2002	.08	1912
2	.05	9566	.05	9206	.05	7998	.04	7478
3	.025	38486	.025	36854	.025	31898	.02	29494
4	.0125	154182	.0125	147634	.0125	127346	.01	118942

**Table 4.:** *Sampling Resolution for each of the Manifolds A–D. Relation between the target distance  $h$  and the number of sample points  $n$  used for each of the manifolds. In each case, the neighbor distances between the points sampled were within  $\approx \pm 30\%$  of the target distance  $h$ .*

## References

- [1] Louis Bachelier. “Théorie de la spéculation”. fr. In: *Annales scientifiques de l’École Normale Supérieure* 3e série, 17 (1900), pp. 21–86. DOI: 10.24033/asens.476. URL: [www.numdam.org/item/ASENS\\_1900\\_3\\_17\\_\\_21\\_0/](http://www.numdam.org/item/ASENS_1900_3_17__21_0/).
- [2] Karl Pearson F.R.S. “LIII. On lines and planes of closest fit to systems of points in space”. In: *The London, Edinburgh, and Dublin Philosophical Magazine and Journal of Science* 2.11 (1901), pp. 559–572. DOI: 10.1080/14786440109462720. eprint: <https://doi.org/10.1080/14786440109462720>. URL: <https://doi.org/10.1080/14786440109462720>.
- [3] G. Klein and Max Born. “Mean first-passage times of Brownian motion and related problems”. In: *Proceedings of the Royal Society of London. Series A. Mathematical and Physical Sciences* 211.1106 (1952), pp. 431–443. DOI: 10.1098/rspa.1952.0051. eprint: <https://royalsocietypublishing.org/doi/pdf/10.1098/rspa.1952.0051>. URL: <https://royalsocietypublishing.org/doi/abs/10.1098/rspa.1952.0051>.
- [4] C. W. Gardiner. *Handbook of stochastic methods*. Series in Synergetics. Springer, 1985.
- [5] R. Abraham, J.E. Marsden, and T.S. Ratiu. *Manifolds, Tensor Analysis, and Applications*. v. 75. Springer New York, 1988. URL: [https://books.google.com/books?id=dWHet\\_zgyCAC](https://books.google.com/books?id=dWHet_zgyCAC).
- [6] Derek Y. C. Chan and Donald A. McQuarrie. “Mean first passage times of ions between charged surfaces”. In: *J. Chem. Soc., Faraday Trans.* 86 (21 1990), pp. 3585–3595. DOI: 10.1039/FT9908603585. URL: <http://dx.doi.org/10.1039/FT9908603585>.
- [7] Kloeden.P.E. and E. Platen. *Numerical solution of stochastic differential equations*. Springer-Verlag, 1992.
- [8] Reinhard Müller, Peter Talkner, and Peter Reimann. “Rates and mean first passage times”. In: *Physica A: Statistical Mechanics and its Applications* 247.1 (1997), pp. 338–356. ISSN: 0378-4371. DOI: [https://doi.org/10.1016/S0378-4371\(97\)00390-7](https://doi.org/10.1016/S0378-4371(97)00390-7). URL: <http://www.sciencedirect.com/science/article/pii/S0378437197003907>.
- [9] L. E. Reichl. *A Modern Course in Statistical Physics*. John Wiley and Sons, 1998.
- [10] M Newman and G Barkema. *Monte carlo methods in statistical physics*. Vol. 24. Oxford University Press: New York, USA, 1999.
- [11] Micheal Spivak. *A Comprehensive Introduction to Differential Geometry*. Ed. by 3. Vol. 1. Publish or Perish Inc., 1999.

- [12] B. Oksendal. *Stochastic Differential Equations: An Introduction*. Springer, 2000.
- [13] Trevor Hastie, Robert Tibshirani, and Jerome Friedman. *Elements of Statistical Learning*. Springer Series in Statistics. New York, NY, USA: Springer New York Inc., 2001.
- [14] A. Pressley. *Elementary Differential Geometry*. Springer, 2001. URL: <https://books.google.com/books?id=UXPyquQa06EC>.
- [15] Sidney Redner. *A Guide to First-Passage Processes*. Cambridge University Press, 2001. DOI: 10.1017/CB09780511606014.
- [16] Per-Olof Persson and Gilbert Strang. “A Simple Mesh Generator in MATLAB”. In: *SIAM Review* 46.2 (2004), pp. 329–345.
- [17] Holger Wendland. *Scattered data approximation*. Vol. 17. Cambridge university press, 2004.
- [18] Michael A. Heroux, Roscoe A. Bartlett, Vicki E. Howle, Robert J. Hoekstra, Jonathan J. Hu, Tamara G. Kolda, Richard B. Lehoucq, Kevin R. Long, Roger P. Pawlowski, Eric T. Phipps, Andrew G. Salinger, Heidi K. Thornquist, Ray S. Tuminaro, James M. Willenbring, Alan Williams, and Kendall S. Stanley. “An Overview of the Trilinos Project”. In: *ACM Trans. Math. Softw.* 31.3 (Sept. 2005), pp. 397–423. ISSN: 0098-3500. DOI: 10.1145/1089014.1089021. URL: <http://doi.acm.org/10.1145/1089014.1089021>.
- [19] John B. Greer, Andrea L. Bertozzi, and Guillermo Sapiro. “Fourth Order Partial Differential Equations on General Geometries”. In: *J. Comput. Phys.* 216.1 (July 2006), pp. 216–246. ISSN: 0021-9991. DOI: 10.1016/j.jcp.2005.11.031. URL: <http://dx.doi.org/10.1016/j.jcp.2005.11.031>.
- [20] Russ Tedrake, Katie Byl, and JE Pratt. “Probabilistic stability in legged systems: Metastability and the mean first passage time (FPT) stability margin”. In: *arXiv* (2006).
- [21] Jérôme Callut and Pierre Dupont. “Learning Partially Observable Markov Models from First Passage Times”. In: *Proceedings of the 18th European Conference on Machine Learning*. ECML ’07. Warsaw, Poland: Springer-Verlag, 2007, 91–103. ISBN: 9783540749578. DOI: 10.1007/978-3-540-74958-5\_12. URL: [https://doi.org/10.1007/978-3-540-74958-5\\_12](https://doi.org/10.1007/978-3-540-74958-5_12).
- [22] J. Hull. *Options, Futures and Other Derivatives*. Prentice Hall finance series. Pearson/Prentice Hall, 2009. ISBN: 9780136015864. URL: <https://books.google.com/books?id=sEmQZoHoJCcC>.
- [23] Richard L. Burden and Douglas Faires. *Numerical Analysis*. Brooks/Cole Cengage Learning, 2010.
- [24] Eric Bavier, Mark Hoemmen, Sivasankaran Rajamanickam, and Heidi Thornquist. “Amesos2 and Belos: Direct and iterative solvers for large sparse linear systems”. In: *Scientific Programming* 20.3 (2012).
- [25] D. Mirzaei, R. Schaback, and M. Dehghan. “On generalized moving least squares and diffuse derivatives”. In: *IMA Journal of Numerical Analysis* 32.3 (2012), pp. 983–1000. ISSN: 0272-4979. DOI: 10.1093/imanum/drr030.
- [26] Óscar Gutiérrez. “American option valuation using first-passage densities”. In: *Quantitative Finance* 13.11 (2013), pp. 1831–1843. DOI: 10.1080/14697688.2013.794387. eprint: <https://doi.org/10.1080/14697688.2013.794387>. URL: <https://doi.org/10.1080/14697688.2013.794387>.

- [27] Jian Liang and Hongkai Zhao. “Solving partial differential equations on point clouds”. In: *SIAM Journal on Scientific Computing* 35.3 (2013), A1461–A1486.
- [28] Thibaud Tallefumier and Marcelo O. Magnasco. “A phase transition in the first passage of a Brownian process through a fluctuating boundary with implications for neural coding”. In: *Proceedings of the National Academy of Sciences* 110.16 (2013), E1438–E1443. ISSN: 0027-8424. DOI: 10.1073/pnas.1212479110. eprint: <https://www.pnas.org/content/110/16/E1438.full.pdf>. URL: <https://www.pnas.org/content/110/16/E1438>.
- [29] E. Ben-Naim and P. L. Krapivsky. “First Passage in Conical Geometry and Ordering of Brownian Particles”. In: *First-Passage Phenomena and Their Applications*. World Scientific, 2014. Chap. Chapter 1, pp. 252–276. DOI: 10.1142/9789814590297\_0011. eprint: [https://www.worldscientific.com/doi/pdf/10.1142/9789814590297\\_0011](https://www.worldscientific.com/doi/pdf/10.1142/9789814590297_0011). URL: [https://www.worldscientific.com/doi/abs/10.1142/9789814590297\\_0011](https://www.worldscientific.com/doi/abs/10.1142/9789814590297_0011).
- [30] Rémy Chicheportiche and Jean-Philippe Bouchaud. “Some Applications of First-Passage Ideas to Finance”. In: *First-Passage Phenomena and Their Applications*. World Scientific, 2014. Chap. Chapter 1, pp. 447–476. DOI: 10.1142/9789814590297\_0018. eprint: [https://www.worldscientific.com/doi/pdf/10.1142/9789814590297\\_0018](https://www.worldscientific.com/doi/pdf/10.1142/9789814590297_0018). URL: [https://www.worldscientific.com/doi/abs/10.1142/9789814590297\\_0018](https://www.worldscientific.com/doi/abs/10.1142/9789814590297_0018).
- [31] T. Chou and M. R. D’Orsogna. “First Passage Problems in Biology”. In: *First-Passage Phenomena and Their Applications*. World Scientific, 2014. Chap. Chapter 1, pp. 306–345. DOI: 10.1142/9789814590297\_0013. eprint: [https://www.worldscientific.com/doi/pdf/10.1142/9789814590297\\_0013](https://www.worldscientific.com/doi/pdf/10.1142/9789814590297_0013). URL: [https://www.worldscientific.com/doi/abs/10.1142/9789814590297\\_0013](https://www.worldscientific.com/doi/abs/10.1142/9789814590297_0013).
- [32] Jonathan J. Hu, Andrey Prokopenko, Christopher M. Siefert, Raymond S. Tuminaro, and Tobias A. Wiesner. *MueLu multigrid framework*. <http://trilinos.org/packages/muelu>. 2014.
- [33] Remy Kusters and Cornelis Storm. “Impact of morphology on diffusive dynamics on curved surfaces”. In: *Phys. Rev. E* 89 (3 2014), p. 032723. URL: <https://link.aps.org/doi/10.1103/PhysRevE.89.032723>.
- [34] Ava J. Mauro, Jon Karl Sigurdsson, Justin Shrake, Paul J. Atzberger, and Samuel A. Isaacson. “A First-Passage Kinetic Monte Carlo method for reaction–drift–diffusion processes”. In: *Journal of Computational Physics* 259 (2014), pp. 536–567. ISSN: 0021-9991. DOI: <https://doi.org/10.1016/j.jcp.2013.12.023>. URL: <http://www.sciencedirect.com/science/article/pii/S002199911300822X>.
- [35] Andrey Prokopenko, Jonathan J. Hu, Tobias A. Wiesner, Christopher M. Siefert, and Raymond S. Tuminaro. *MueLu User’s Guide 1.0*. Tech. rep. SAND2014-18874. Sandia National Labs, 2014.
- [36] Cenk Oguz Saglam and Katie Byl. “First Passage Value”. In: *arXiv* (2014). arXiv: 1412.6704 [cs.SY].

- [37] O Bénichou, T Guérin, and R Voituriez. “Mean first-passage times in confined media: from Markovian to non-Markovian processes”. In: *Journal of Physics A: Mathematical and Theoretical* 48.16 (2015), p. 163001. DOI: 10.1088/1751-8113/48/16/163001. URL: <https://doi.org/10.1088/1751-8113/48/16/163001>.
- [38] Nicholas F. Polizzi, Michael J. Therien, and David N. Beratan. “Mean First-Passage Times in Biology.” eng. In: *Israel journal of chemistry* 56 (9-10 2016), pp. 816–824.
- [39] Jon Karl Sigurdsson and Paul J. Atzberger. “Hydrodynamic coupling of particle inclusions embedded in curved lipid bilayer membranes”. In: *Soft Matter* 12.32 (2016), pp. 6685–6707. ISSN: 1744-683X. URL: <http://dx.doi.org/10.1039/C6SM00194G>.
- [40] Khem Raj Ghusinga, John J. Dennehy, and Abhyudai Singh. “First-passage time approach to controlling noise in the timing of intracellular events”. In: *Proceedings of the National Academy of Sciences* (2017). ISSN: 0027-8424. DOI: 10.1073/pnas.1609012114. eprint: <https://www.pnas.org/content/early/2017/01/04/1609012114.full.pdf>. URL: <https://www.pnas.org/content/early/2017/01/04/1609012114>.
- [41] B. Gross and P. J. Atzberger. “Spectral Numerical Exterior Calculus Methods for Differential Equations on Radial Manifolds”. In: *Journal of Scientific Computing* (2017). ISSN: 1573-7691. DOI: 10.1007/s10915-017-0617-2. URL: <https://doi.org/10.1007/s10915-017-0617-2>.
- [42] C. Hohenegger, R. Durr, and D.M. Senter. “Mean first passage time in a thermally fluctuating viscoelastic fluid”. In: *Journal of Non-Newtonian Fluid Mechanics* 242 (2017), pp. 48–56. ISSN: 0377-0257. DOI: <https://doi.org/10.1016/j.jnnfm.2017.03.001>. URL: <http://www.sciencedirect.com/science/article/pii/S0377025717301106>.
- [43] Alan E. Lindsay, Andrew J. Bernoff, and Michael J. Ward. “First Passage Statistics for the Capture of a Brownian Particle by a Structured Spherical Target with Multiple Surface Traps”. In: *Multiscale Modeling & Simulation* 15.1 (2017), pp. 74–109. DOI: 10.1137/16M1077659. eprint: <https://doi.org/10.1137/16M1077659>. URL: <https://doi.org/10.1137/16M1077659>.
- [44] Aaron Meurer, Christopher P. Smith, Mateusz Paprocki, Ondřej Čertík, Sergey B. Kirpichev, Matthew Rocklin, AMiT Kumar, Sergiu Ivanov, Jason K. Moore, Sartaj Singh, Thilina Rathnayake, Sean Vig, Brian E. Granger, Richard P. Muller, Francesco Bonazzi, Harsh Gupta, Shivam Vats, Fredrik Johansson, Fabian Pedregosa, Matthew J. Curry, Andy R. Terrel, Štěpán Roučka, Ashutosh Saboo, Isuru Fernando, Sumith Kulal, Robert Cimrman, and Anthony Scopatz. “SymPy: symbolic computing in Python”. In: *PeerJ Computer Science* 3 (Jan. 2017), e103. ISSN: 2376-5992. DOI: 10.7717/peerj-cs.103. URL: <https://doi.org/10.7717/peerj-cs.103>.
- [45] Ka Chun Cheung and Leevan Ling. “A kernel-based embedding method and convergence analysis for surfaces PDEs”. In: *SIAM Journal on Scientific Computing* 40.1 (2018), A266–A287.
- [46] S. Debnath, L. Liu, and G. Sukhatme. “Solving Markov Decision Processes with Reachability Characterization from Mean First Passage Times”. In: *2018 IEEE/RSJ International Conference on Intelligent Robots and Systems (IROS)*. 2018, pp. 7063–7070. DOI: 10.1109/IROS.2018.8594383.

- [47] Denis S. Grebenkov, Ralf Metzler, and Gleb Oshanin. “Strong defocusing of molecular reaction times results from an interplay of geometry and reaction control”. In: *Communications Chemistry* 1.1 (Dec. 2018), p. 96. ISSN: 2399-3669. URL: <https://doi.org/10.1038/s42004-018-0096-x>.
- [48] B.J. Gross and P.J. Atzberger. “Hydrodynamic flows on curved surfaces: Spectral numerical methods for radial manifold shapes”. In: *Journal of Computational Physics* 371 (2018), pp. 663–689. ISSN: 0021-9991. DOI: <https://doi.org/10.1016/j.jcp.2018.06.013>. URL: <http://www.sciencedirect.com/science/article/pii/S0021999118303917>.
- [49] Adam Kells, Zsuzsanna É. Mihálka, Alessia Annibale, and Edina Rosta. “Mean first passage times in variational coarse graining using Markov state models”. In: *The Journal of Chemical Physics* 150.13 (2019), p. 134107. DOI: 10.1063/1.5083924. eprint: <https://doi.org/10.1063/1.5083924>. URL: <https://doi.org/10.1063/1.5083924>.
- [50] Paul Kuberry, Peter Bosler, and Nathaniel Trask. *Compadre Toolkit*. Tech. rep. Sandia National Laboratories, Jan. 2019. DOI: 10.11578/dc.20190411.1. URL: <https://github.com/SNLComputation/compadre>.
- [51] Junhong Xu, Kai Yin, and Lantao Liu. “Reachable Space Characterization of Markov Decision Processes with Time Variability”. In: (2019). arXiv: 1905.09342 [cs.RD].
- [52] B.J. Gross, N. Trask, P. Kuberry, and P. J. Atzberger. “Meshfree methods on manifolds for hydrodynamic flows on curved surfaces: A Generalized Moving Least-Squares (GMLS) approach”. In: *Journal of Computational Physics* 409 (2020). URL: <https://doi.org/10.1016/j.jcp.2020.109340>.
- [53] Nathaniel Trask and Paul Kuberry. “Compatible meshfree discretization of surface PDEs”. In: *Computational Particle Mechanics* 7.2 (Mar. 2020), pp. 271–277. ISSN: 2196-4386. URL: <https://doi.org/10.1007/s40571-019-00251-2>.